Supplementary Material

AE/Fe-MOF/PVDF Heterojunction Self-cleaning Photocatalytic Membrane for Rapid Electron Transfer to Enhance Photo-Fenton Degradation of Tannic Acid

Jiajia Li[a*], Yulu Liu[a], Manhua Chen[a], Keke Cao[a], Rongqiang Zhang[a], Nan Zhang[a], Zhi Li[a], Qi Qiang[a], Yuping Tang[a*], Qizhao Wang[b*]

[a] *Key Laboratory of Shaanxi Administration of Traditional Chinese Medicine for TCM Compatibility, Shaanxi University of Chinese Medicine, Xianyang 712046, Shaanxi Province, China.*

[b] *School of Water and Environment, Key Laboratory of Subsurface Hydrology and Ecological Effects in Arid Region of Ministry of Education, Chang'an University, Xi'an, 710064, China*

**Corresponding authors.*

E-mail addresses: ljjzhw2017@sntcm.edu.cn (J. Li), yupingtang@sntcm.edu.cn (Y. Tang), qzwang@chd.edu.cn (Q. Wang).

Text S1. Supplemental experimental

Text S1.1 Materials and chemicals

Polyvinylidene fluoride (PVDF) membrane UF050, purchased from Zhong Ke Ruiyang Membrane Technology Company, was cut into discs with a diameter of 75 mm and a filtration area of 41.8 cm^2 to serve as the substrate for this study. Ferric chloride hexahydrate ($FeCl_3 \cdot 6H_2O$) and o-phthalic acid were obtained from Shanghai Macklin Biochemical Technology Co., Ltd. and Shanghai Aladdin Biochemical Technology Co., Ltd. N,N-Dimethylformamide (DMF) was supplied by Tianjin Fuyu Fine Chemical Co., Ltd. *Rheum officinale* Baill. and *Polygonum cuspidatum* Sieb. et Zucc. were provided by the Pharmaceutical Factory of Shaanxi University of Traditional Chinese Medicine. All chemical reagents were used as received without further purification.

Text S1.2 Membrane performance

The ultrafiltration membrane component is the stirred ultrafiltration unit (Amicon Stirred Cell, UFSC40001), which operates in dead-end filtration mode. It is equipped with a magnetic stirring paddle, and external pressure is supplied via the high-purity nitrogen gas cylinder. The effective membrane area is 41.8 cm^2 for all membrane sheets, and all membranes are stored at 4°C.

The membranes were affixed within the dead-end filtration apparatus. The pure water permeability (J_{w0}), as well as the fluxes of the TA solution and herbal wastewaters (Jp), were then measured at a constant operating pressure of 1 bar. All flux values were calculated using Equation (1) and are reported in standardized units of L m^{-2} h^{-1} bar^{-1}.

The water permeability (J) was calculated using Equation (1):

$$J = \frac{V}{A \times \Delta t \times P} \quad (1)$$

For the calculation of water permeability (J), several critical parameters were utilized where A represents the effective filtration area in square meters (m^2), Δt is the filtration time in hours (h), P denotes the applied operating pressure in bars (bar), and V corresponds to the permeate volume collected during the time period Δt, measured in liters (L).

Under standard ambient conditions (25°C, 1 bar), xenon lamp with wavelength cutoff ≥ 420 nm was employed. Next, the 0.01 M H_2O_2 solution was added to the photo-Fenton system, which was used to treat the fouled membrane over 30-minute duration. Following the photo-Fenton purification step, the membrane underwent further 30-minute filtration with pure water, and the osmotic flux measured during this process was designated as J_{w1}, representing the membrane's flux after photo-Fenton cleaning.

The anti-fouling behavior of the as-synthesized membranes was characterized using the flux recovery ratio (FRR), as determined by the equation that follows:

$$FRR = \frac{J_{w1}}{J_{w0}} \times 100\% \quad (2)$$

The fouling process was additionally characterized by means of the total fouling ratio (R_t), reversible fouling ratio (R_r), and irreversible fouling ratio (R_{ir}), with these parameters calculated using the following equations:

$$R_r = \frac{J_{w1} - J_p}{J_{w0}} \quad (3)$$

$$R_{ir} = \frac{J_{w0} - J_{w1}}{J_{w0}} \quad (4)$$

$$R_t = R_r + R_{ir} \quad (5)$$

Text S1.3 AE/Fe-MOF/PVDF characterization

The morphological structure and corresponding elemental mappings were meticulously examined by a field emission scanning electron microscope (ZEISS sigma300) and transmission electron microscope (TEM JEOL JEM-F200) that operated at an accelerated voltage of 200 kV. The atomic force microscopy (AFM) tests were conducted utilizing a Bruker Dimension Icon system from Germany. Powder X-ray diffraction (XRD) patterns were meticulously acquired with an X'Pert PRO MPD advanced diffractometer, with a scanning rate of 2° per minute. Fourier-transform infrared spectroscopy (FT-IR) analysis was performed using equipment from Brooke, Germany. The chemical composition of the samples was analyzed by an X-ray photoelectron spectrometer (Axis Ultra DLD). UV-visible diffuse reflectance spectroscopy (UV-Vis DRS) was carried out using an Agilent Cary-5000 UV-Vis spectrophotometer. Photoelectrochemical (PEC) measurements were taken utilizing a CHI-760E electrochemical workstation produced by Shanghai Chen Hua Corporation. BET was tested using MicroActive 5.02 and zeta potential on solid membrane surface was tested using Anton Paar surpass3 from Austria. For LC-MS fragmentation information, a Thermo Fei Ultimate 3000 UHPLC-Q Exactive system was employed.

Text S1.4 Catalytic Degradation properties and capture tests

Degradation experiments were conducted in a 500 mL glass beaker. The total solution volume was 85 mL, with the initial hour dedicated to dark reaction adsorption

followed by the subsequent hour for photo-Fenton degradation. Illumination was provided by a 500 W xenon lamp (CEL-S500/350, China education Au-Light) emitting visible light with a wavelength of $\lambda \geq 420$ nm, while a 400 nm cutoff filter was utilized. At 15-minute intervals, approximately 5 mL samples were withdrawn, and filtered through a needle filter with a pore size of 0.45 μm, and their concentration was assessed at 277 nm using a UV-Vis spectrophotometer (Shimazu UV-1780). The catalytic degradation performance of the composite membrane was assessed under various molar ratios, concentrations of tannin, and pH levels. The pH of the solution was adjusted using 0.01 mol/L sulfuric acid and sodium hydroxide. Furthermore, the stability of the photocatalyst was evaluated through multiple cycling experiments, offering valuable insights into the catalyst's performance with repeated use. Isopropanol (IPA), p-benzoquinone (BQ), ammonium oxalate (AO), silver nitrate ($AgNO_3$), and L-histidine (L-his) at a concentration of 10 mmol/L were employed as scavengers for hydroxyl radicals (•OH), superoxide radicals ($\bullet O_2^-$), holes (h^+), electrons (e^-), and singlet oxygen ($^1O_2$), respectively. The COD content is analyzed using a water quality analyzer (5B-3C(V8), Beijing Lianhua Technology), providing an assessment of the COD levels in wastewater from TA, *Ploygonum cuspidatum* Sieb. et Zucc., and *Rheum officinale* Baill.

Text S2. Supplemental experimental results and discussion

Figure S1. (a) High-resolution XPS spectra of (a) O 1s, (b) F 1s.

Figure S2. Mott-Schottky plots of pure and composite samples.

Figure S3. R^2 values of (a) intermediate blocking, (b) standard blocking mode and (c) complete blocking model fitted with Hermia classic model for patchouli oil under the different filtration time.

Figure S4. Determination of pseudo-first-order rate constant for NB degradation in the AE/Fe-MOF membrane system under light irradiation.

Figure S5. First-order kinetic plot of Fe^{2+} generation in the AE/Fe-MOF/PVDF membrane system.

Figure S6. (a) EPR analysis of hydroxyl radical (•OH), (b) superoxide radical ($•O_2^-$).

Figure S7. LC-MS spectra of Gallic acid, Benzene carboxylic acid, 1,2,3,5-Substituted tetrahydroxybenzene, (d) Pyrogallic acid, Ethanedioic acid and Maleinic acid.

Table S1. Comparison of pollutant degradation performance of various MOF-based catalysts reported in recent literature.

Table S2. Performance comparison of various reported and commercial membranes in terms of flux and antifouling properties.

Table S3. Fe leaching concentrations of the AE/Fe-MOF/PVDF membrane at different stages.

Table S4. Specific surface areas and pore characteristics of different samples.

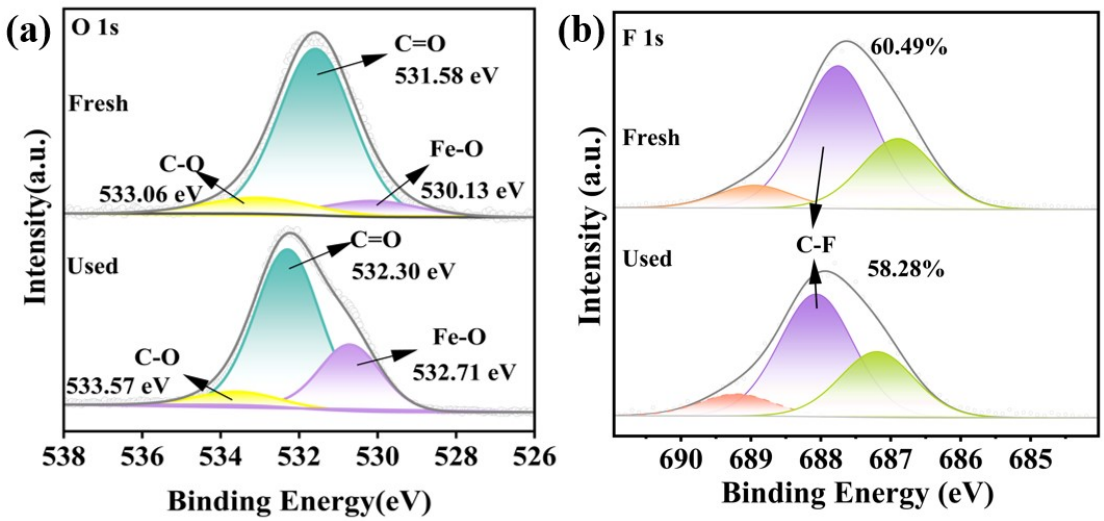

Figure S1. (a) High-resolution XPS spectra of (a) O 1s, (b) F 1s.

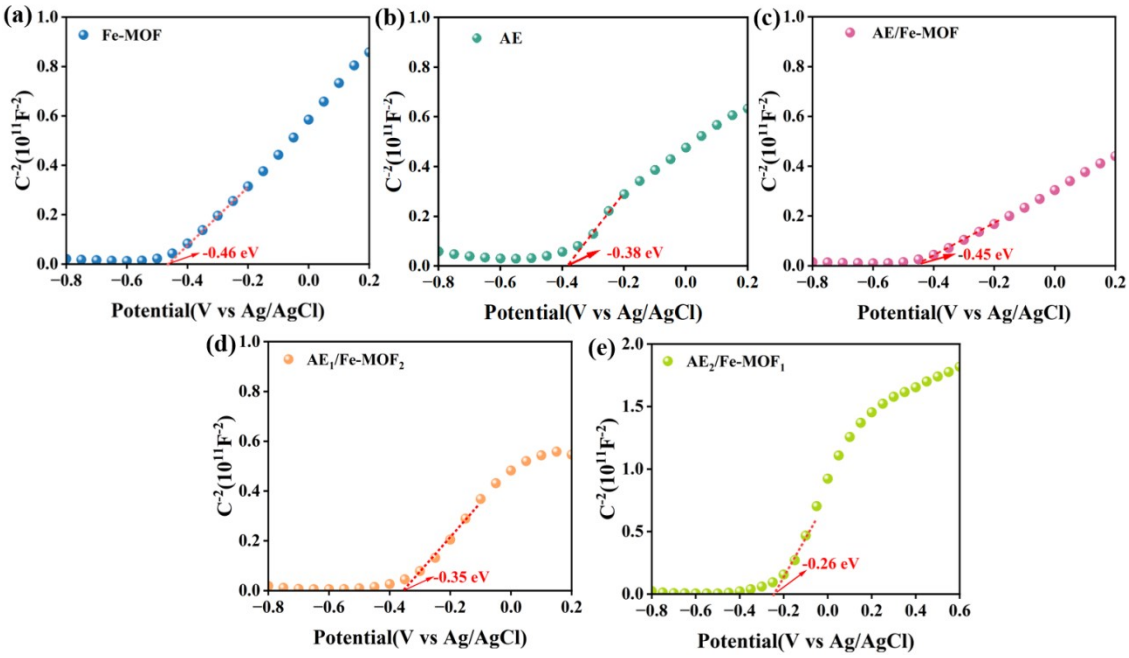

Figure S2. Mott-Schottky plots of pure and composite samples

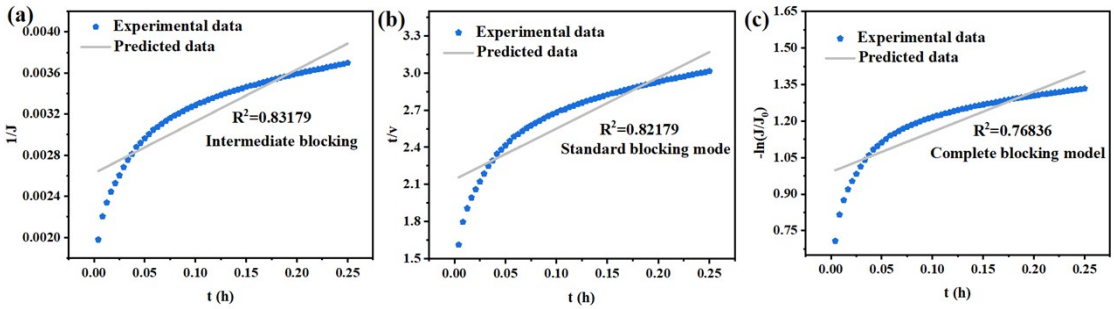

Figure S3. R^2 values of (a) intermediate blocking, (b) standard blocking mode and (c) complete blocking model fitted with Hermia classic model for patchouli oil under the different filtration time.

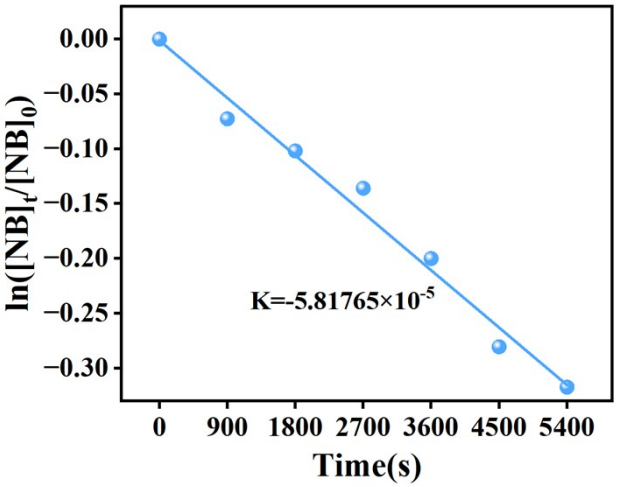

Figure S4. Determination of pseudo-first-order rate constant for NB degradation in the AE/Fe-MOF membrane system under light irradiation.

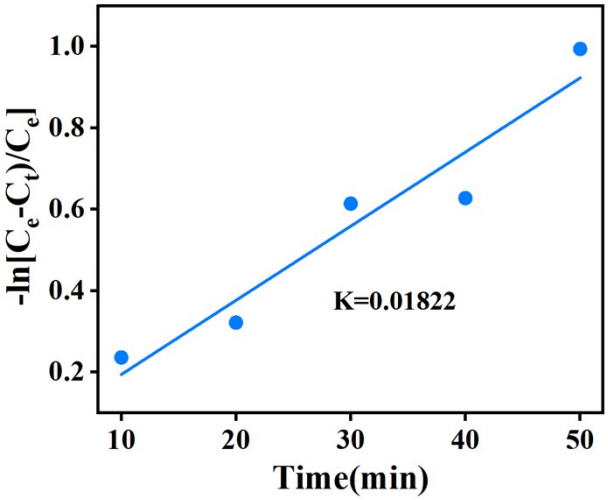

Figure S5. First-order kinetic plot of Fe^{2+} generation in the AE/Fe-MOF/PVDF membrane system.

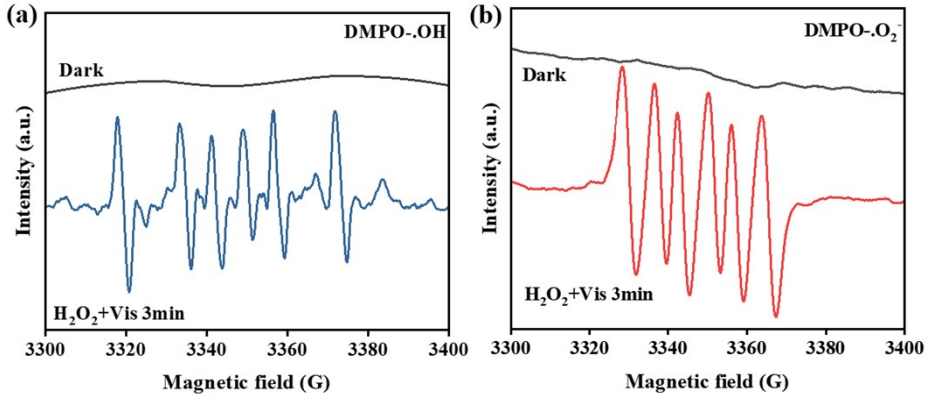

Figure S6. (a) EPR analysis of hydroxyl radical (•OH), (b) superoxide radical ($•O_2^-$).

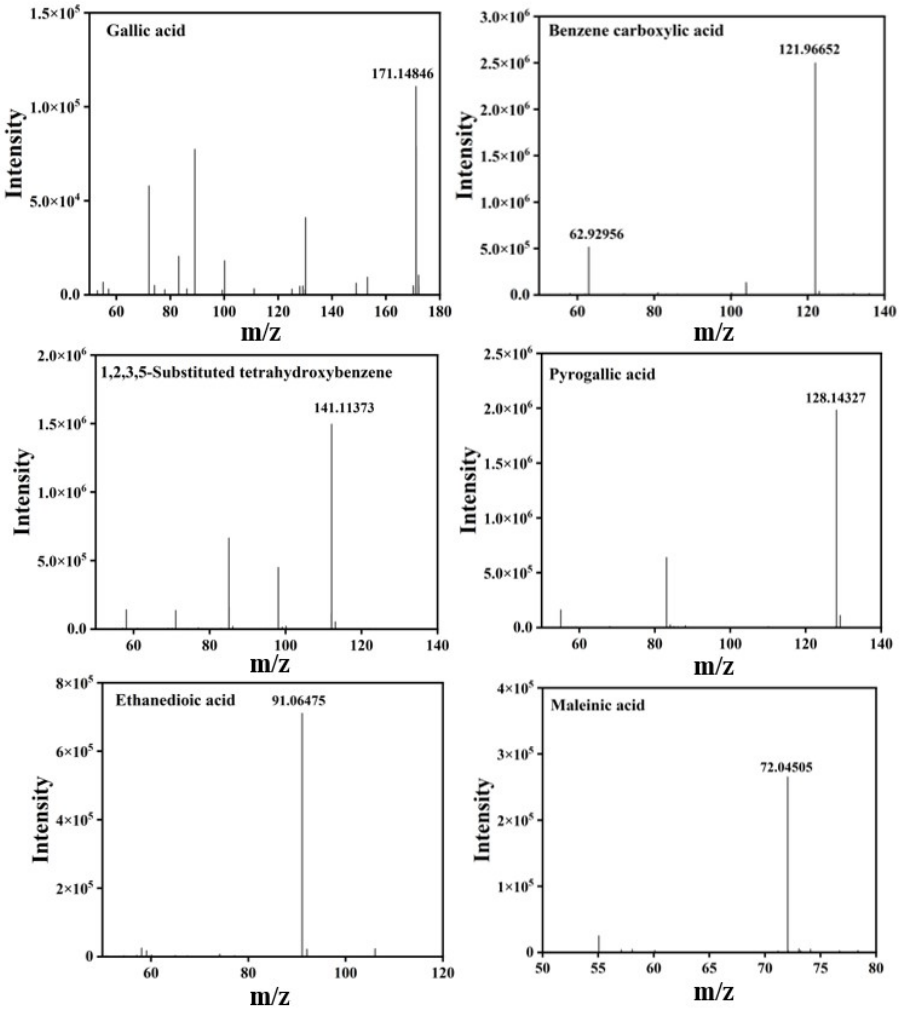

Figure S7. LC-MS spectra of Gallic acid, Benzene carboxylic acid, 1,2,3,5-Substituted tetrahydroxybenzene, Pyrogallic acid, Ethanedioic acid and Maleinic acid.

Table S1. Comparison of pollutant degradation performance of various MOF-based catalysts reported in recent literature.

Catalyst	Pollutant	Degradation (%)	Time (min)	Reaction System	Reference
AE/Fe-MOF	TA	87.29	90	Photo-Fenton	This work
g-C_3N_4@a-Fe-MOF	DOX	96.8	60	Photo-Fenton	[1]
Fe-MOF-NH_2	OFX	97	100	Visible-light photocatalysis	[2]
Fe(II)-MOF-CA	SMX	91.96	120	PS activation	[3]
Fe-MOFs-2	SMX	95	120	PS activation	[4]
La-MOF	RhB	91.3	100	PMS activation	[5]

Table S2. Performance comparison of various reported and commercial membranes

in terms of flux and antifouling properties.

Membrane	Pollutant tested	Pure water flux (L m^{-2} h^{-1} bar^{-1})	Pollutant flux (L m^{-2} h^{-1} bar^{-1})	FRR (%)	Reference
AE/Fe-MOF/ PVDF	Tannic acid	694.31	477.56	96.5	This work
MCOC/PVDF	HA/phenol	649	272(HA)	85(phenol)	[6]
NH_2-MIL-101(Fe)-CNC@PVDF	TBBPA	815.41	-	-	[7]
ZnL-PVDF	BSA (for rejection)	271.8	-	96.5	[8]
JM200	Multiple EOCs	55.6	-	90.7	[9]

Table S3. Fe leaching concentrations of the AE/Fe-MOF/PVDF membrane at different stages.

Operation stage	Fe leaching concentration (ug/L,n=3)			Average Fe leaching concentration(ug/L)
Initial 60-min filtration	42.6803	43.3536	42.2449	42.76
After the 3rd cycle	106.6650	103.0756	103.9573	104.57
After the 6th cycle	189.3295	188.2358	183.8593	187.14

Table S4. Specific surface areas and pore characteristics of different samples

Samples	S_{BET}	Pore volume
AE/Fe-MOF/PVDF	($m^2.g^{-1}$)	($cm^3.g^{-1}$)
After filtering tannic	4.1921	0.029539
After the photo-Fenton	4.5902	0.033634

References

[1] J.X. Liu, J.H. Tang, Q. Dang, X.D. Duan, F.C. Wei, W. Zhang, L. Tang and M.H. Wu, Sep. Purif. Technol., 2026, 385, 136394, DOI:org/10.1016/j.seppur.2025.136394.

[2] H.L. Wang, H.S. Cui, Y. Lan, L.P. Yang, J.H. Zhao, Y.T. Ye, W.J. Zhang, R.J. Deng, H.J. Liu, Y. Lv and H. Yang, J. Colloid Interface Sci., 2025, 695, 137797,

DOI:org/10.1016/j.jcis.2025.137797.

[3] H.J. Chen, J.Q. Wan, Z.C. Yan, Y.W. Ma, Y. Wang, Y.C. Xie and J. Hou, J. Clean. Prod., 2022, 348, 131367, DOI:org/10.1016/j.jclepro.2022.131367.

[4] J. Sun, J.Q. Wan, Y. Wang, Z.C. Yan, Y.W. Ma, S. Ding, M. Tang and Y.C. Xie, J. Hazard. Mater., 2022, 429, 128299, DOI:org/10.1016/j.jhazmat.2022.128299.

[5] J.Q. Li, S. Zhang, P.Y. Sun, J.F. Li, T.T. Sun, R.Q. Guan, F.M. Zeng and C.B. Liu, ACS Omega., 2026, 11, 3195-3204, DOI:org/10.1021/acsomega.5c09875.

[6] H. Jiang, L.F. Zhang, C.T. Zhang, X.M. Xiao, Z.Z. Tian and Y.L. Sun, J. Water Process Eng., 2024, 57, 104635, DOI:org/10.1016/j.jwpe.2023.104635.

[7] X. Ji, Z.X. Wu, Y.H. Liu, Y.W. Kou, X.D. Li, W.-X. Zhang and Z.L. Deng, Chem. Eng. J., 2025, 518 164521, DOI:org/10.1016/j.cej.2025.164521.

[8] W. Wang, Y.P. Shi, P. Zhang, Z.C. Zhang and X. Xu, J. Phys. Chem. .Solids, 2022 171, 110865, DOI:org/10.1016/j.jpcs.2022.110865.

[9] Z.B. Hu, K.Y. Tian, L.Z. Li, H. Dai, Z.B. Peng, Z.L. Yin and W.B. Yang, Chem. Sci., 2026, 17, 1137, DOI:org/10.1039/d5sc05978j.